A Cantilever-Based Method for Probing Adhesive Force and Detachment Energy in Cohesive Granular Materials

Maxime Lajeunesse, Francisco M Rocha, Denis Dumont, Vincent Bertin, Yoahn Moratille, Nathalie Sintes-Zydowicz, Eric Drockenmuller, Olivier Pouliquen

A Cantilever-Based Method for Probing Adhesive Force and Detachment Energy in Cohesive Granular Materials

Maxime Lajeunesse[a], Francisco M. Rocha[a,b], Denis Dumont[a], Vincent Bertin[c], Yoahn Moratille[d], Nathalie Sintes-Zydowicz[d], Eric Drockenmuller[d], Olivier Pouliquen[a]

[a] *Aix Marseille University, CNRS, IUSTI, Marseille, France*
[b] *Institut Franco-Argentin de Dynamique des Fluides pour l'Environnement (IFADyFE), CNRS IRL 2027, University of Buenos Aires, CONICET, Buenos Aires, Argentina*
[c] *Université Côte d'Azur, CNRS, INPHYNI , Nice, France*
[d] *Université Lyon 1 Claude Bernard, CNRS, Ingénierie des Matériaux Polymères, UMR 5223, Villeurbanne, France*

Abstract

Interparticle adhesion plays a critical role in the flow behavior of cohesive granular materials, yet quantitative characterization at the particle scale remains challenging. Here, we present a versatile cantilever-based method that combines a glass-beam cantilever for force measurements with a novel catapult mode for energy measurements, enabling the determination of both detachment force and detachment energy. Applied to three different cohesive materials: polymer-coated silica particles, wet granular media, and cross-linked poly(2-ethylhexyl acrylate) (PEHA) microparticles, this method reveals a fundamental decoupling between force and energy, suggesting that both quantities are equally critical for characterizing grain properties.

Keywords: Adhesion, Cohesive Granular Materials, Cantilever Force Measurements, Microparticles

1. Introduction

While substantial progress has been made in understanding and modeling dry granular materials [1], predicting the flow of cohesive granular materials, such as wet sand, snow, and powders, remains a significant scientific challenge [2–5]. These materials are ubiquitous in industry, where issues like jamming, clogging, and flow localization pose serious challenges for process optimization and product manufacturing. Cohesive granular materials are also central to large-scale geophysical flows, such as debris flows and snow avalanches, which are among the most dangerous natural hazards, threatening both people and infrastructure.

Adhesion between particles can arise from various physical interactions, including van der Waals forces, capillary bridges, or chain entanglement in the case of polymer-coated particles. A major challenge lies in linking these microscopic interactions to macroscopic flow behavior [6–8]. A critical first step toward addressing this challenge is to accurately characterize interparticle interactions, enabling their control and providing insight into their connection to rheological properties [9]. In this paper, we propose simple yet powerful innovative experimental method to accurately measure both adhesive detachment forces and detachment energy between adhesive particles, a crucial milestone towards a better understanding of the flow behavior of cohesive granular materials.

Despite their importance, measurements of adhesive properties at the particle scale are scarce in powder technology. For sufficiently large particles ($d > 1$ mm), sensitive force sensors can be used to measure the force required to

Email address: olivier.pouliquen@univ-amu.fr (Olivier Pouliquen[a])

detach two particles in contact [9, 10]. For smaller particles ($d < 100$ μm), Atomic Force Microscopy (AFM) is an efficient alternative. AFM has been extensively developed and used in the suspensions and colloids community to accurately probe particle properties [11–13]. For dry particles and powders, the use of AFM is less common but has been employed in several studies [6, 14–16]. By attaching one particle to the AFM cantilever and another to a substrate, it is possible to probe adhesive detachment forces. However, this technique is relatively tedious, limited to particles smaller than the typical size of AFM cantilevers ($d < 100$ μm), and does not easily allow for a large number of measurements to obtain meaningful statistics.

Other approaches have been developed for layers of grains rather than individual particles, enabling adhesion measurements between a surface and a large number of particles. One technique involves placing grain-covered plates in a centrifuge and observing grain detachment as the rotational speed gradually increases [17, 18]. Another method consists of subjecting the plate to an impact and counting the number of grains detached [19–21]. While these methods provide estimates of the adhesive forces at play, they lack accuracy in characterizing interparticle interactions.

In this study, we present a new method to measure and characterize the adhesive properties of particles in the 100μm-1mm range. We sought a more versatile approach than AFM, enabling large-scale statistical measurements. The method is largely inspired by techniques used in biophysics for probing cell responses to small forces, where a thin glass beam is used as a cantilever [22, 23]. We demonstrate that this method allows for easy characterization of numerous particles and provides statistical insights. Additionally, we modified the setup to function as a catapult, measuring the minimum launching velocity necessary to detach one particle from another. This measurement resembles percussion experiments proposed in the literature [20, 21] to estimate adhesion between a surface and particles but is adapted for single pairs of particles. This approach provides a measure of detachment energy, which has been suggested as a crucial parameter governing powder flow properties [24–28] but has yet to be thoroughly documented.

To demonstrate the versatility of our method, we apply these techniques to analyze the adhesive properties of various model cohesive materials where adhesion stems from different origins. We analyze polymer-coated silica particles, a controlled cohesive granular material (CCGM) recently proposed to create sticky particles where adhesion is controlled by the coating thickness [29]. We also probe wet particles, where small amounts of liquid are mixed within the medium, inducing the formation of capillary bridges between individual grains [30–32]. The last material used in this study consists of synthesized polymer particles [33], obtained through membrane emulsification, whose mechanical properties differ from the others by being much softer.

The paper is organized as follows. In Section 2, we describe the adhesive particles used throughout the study. In Section 3, we detail the experimental setup designed to measure adhesion forces between cohesive grains and present the results for the CCGM particles. Section 4 describes how the setup was adapted to assess detachment energies. Finally, in Section 5, we demonstrate the versatility of our method by applying it to other cohesive materials described above.

2. The Adhesive Particles

Experiments were performed using three cohesive granular materials, each exhibiting a different origin of interparticle adhesion.

The first material consists of spherical glass particles coated with a thin layer of polyborosiloxane (PBS). For millimeter-sized particles, the adhesive force between two Cohesion-Controlled Granular Material (CCGM) particles has been shown to depend on the average thickness b of the PBS coating [29]. Here, we extend this approach to silica particles with

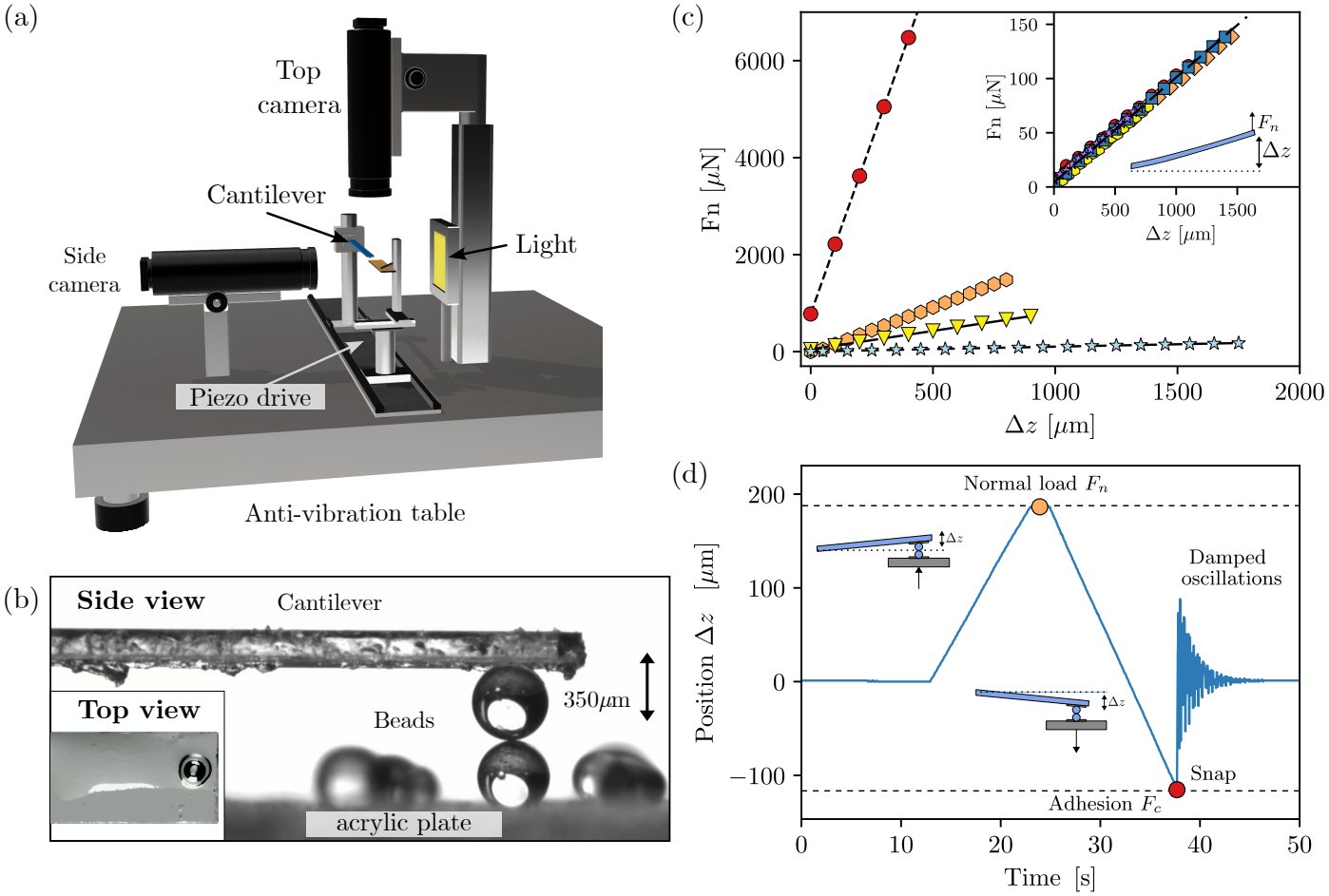

Figure 1: (a) Sketch of the experimental cantilever setup. (b) Side and top views of a typical field of view during force measurements. (c) Calibration of the force-deflection relationship for glass beams (width $w = 1$mm) with varying thickness e and length L; $e = 400\,\mu$m and $L = 8$ cm (red circles); $e = 400\,\mu$m and $L = 6$ cm (orange diamonds); $e = 145\,\mu$m and $L = 8$ cm (yellow triangles); $e = 145\,\mu$m and $L = 6$ cm (blue stars). Dashed lines show predictions from Eq. 1. Inset: Reproducibility test for four beams with identical geometry ($e = 145\,\mu$m and $L = 6$ cm) providing the cantilever stiffness $k = 0.095 \pm 0.002$ N/m. (d) Time evolution of the vertical deflection Δz measured by the side camera during one attachment-detachment cycle between two particles.

diameters $d = 199 \pm 16$ μm and 350 ± 67 μm, and average PBS coating thicknesses ranging from 0 to 140 nm, prepared according to the protocol described earlier [29]. Particles are first mixed with boric acid dissolved in purified water heated at 60°C and the PDMS. The mixture is stirred during 90 minutes in a mixer at 110°C to evaporate the water. At the end of the process, the polymer cross links with the silica particles and creates a quasi homogeneous coating. We provide a more detailled explanation of the coating process in Appendix A.

The second material consists of the same glass beads with $d = 199 \pm 16\,\mu$m mixed with a Newtonian, non-volatile liquid composed of 60wt% glycerol and 40wt% water. The medium was prepared by adding liquid corresponding to 0.1 wt.% of the particle mass and thoroughly mixing the system to obtain a wet granular medium in the funicular regime, where interparticle adhesion arises from liquid capillary bridges [31, 32].

The third material consists of cross-linked PEHA microparticles synthesized using a procedure adapted from earlier work [33], with averaged diameter d = 232 μm. The microparticles are composed of tailor-made cross-linked poly(2-ethylhexyl acrylate) (PEHA) and

are obtained through membrane emulsification-assisted suspension radical copolymerization. The synthesis of these polymer microparticles is fully detailed in Appendix B. Since the glass transition temperature of PEHA is below ambient temperature (T_g = -59 °C), the particles are relatively soft. The Young's modulus, estimated from nanoindentation, is approximately E = 5.2MPa, which is 10^4 times smaller than the glass particles for which $E = 50$GPa.

3. Measuring Adhesion Force

3.1. Experimental Setup

Classical methods for measuring adhesive forces often rely on cantilevers, i.e., elastic beams whose deformation provides a measure of the applied force. This principle underlies conventional Atomic Force Microscopy (AFM), in which cantilever deflection is accurately measured by tracking the displacement of a reflected laser beam. Our experimental setup, shown in Fig.1a, is based on a cantilever design inspired by systems developed for probing cell mechanics [23, 34].

The cantilever consists of a thin glass beam with a length of 6-8 cm, width of 1 mm, and thickness of 145-400 μm. These dimensions can be adjusted to tune the cantilever stiffness to the expected force range. One end of the cantilever is fixed to a vertical support, while a grain is attached to the free end using a repositionable adhesive (3M RePositionable 75). The adhesive strength of the glue is significantly larger than the interparticle adhesive forces being measured, while remaining low enough to allow easy removal and replacement of the attached grain.

Below the cantilever, a monolayer of grains is fixed onto an acrylic plate mounted on a 3D micro-piezo translation stage (micronix PPS-20), enabling vertical motion of the particle layer. The stage can be operated manually via a joystick for approach and positioning, or automatically through computer control to perform measurement cycles.

Two DMK Imaging Source cameras equipped with Leica Z16 lenses provide high-resolution side and top-view imaging (1.5 micron/pix) to ensure particle alignment [Fig. 1b] and continuously measure cantilever deflection. LED backlighting provides high contrast for accurate particle tracking. The entire setup is mounted on an anti-vibration table to minimize mechanical noise.

The experiment operates like an AFM, with detachment forces inferred from measurements of cantilever deflection. However the simplicity of our setup allows many (bottom and top) particles to be probed without changing the cantilever. This turns out to be crucial for performing relevant statistical analysis on the measured force for our coated particles.

3.2. Characterising the glass beam cantilever

One strength of the experimental setup is its ability to measure a wide range of forces by appropriately selecting the cantilever geometry. The accessible force range is determined by the cantilever stiffness and the camera field of view. In practice, these parameters are adjusted so that the maximum cantilever deflection at detachment remains within the camera field of view, usually set with a height between 1 or 2 mm.

The cantilever stiffness k is given by beam theory [35]:

$$k = E\frac{we^3}{4L^3}\,, \tag{1}$$

where e is the beam thickness, L the length, w its width and E its Young's modulus.

To characterize the accessible stiffness range, we varied the beam thickness e from 145 to 400 μm and the length L from 6 to 8 cm, while keeping the width constant at w = 1 mm. We measured the force as a function of deflection using a precision scale. The results, shown in Fig.1c, demonstrate that the stiffness can be varied over two orders of magnitude, ranging from 0.10 to 14.25 Nm^{-1}, following the predicted law given by eq.1. We also verified that different glass beams with the same geometry exhibit the same stiffness (Fig.1c).

Unless otherwise specified, a glass beam with L = 8 cm, e = 0.145 mm, and w = 1 mm was used for most of the adhesive force measurements. The camera field of view sets the

maximum measurable deflection, corresponding to a maximum force of 200 μN. With a camera resolution of 1.5 micron/pix, the minimum detectable force is approximately 0.2 μN. The setup therefore allows force measurements over a range spanning approximately three orders of magnitude, from 0.2 to 200 μN.

3.3. Experimental protocol for force measurements

The first step of the protocol involves fixing the particles. A small amount of repositionable adhesive is applied to the cantilever tip over a region of approximately 1 mm in length, and a thin layer of the same adhesive is sprayed onto the base plate. One particle is then attached to the free end of the cantilever, while a monolayer of particles is fixed to the acrylic base plate. The cantilever is then clamped to the vertical support, and the acrylic plate is mounted on the 3D piezo stage.

Once the particles are mounted, top and side-view images, combined with joystick control, are used to align the particle attached to the cantilever with a particle on the substrate, as shown in Fig.1b. When the two particles are vertically aligned, the measurement procedure begins. The acrylic plate is first raised, bringing the particles into contact and producing an upward deflection of the cantilever by a magnitude Δz from its equilibrium position. This generates a normal force $F_n = k\Delta z$, which reaches its maximum value at the maximum vertical displacement of the cantilever, as depicted by the yellow circle in Fig.1d.

The plate is subsequently lowered, reducing the cantilever deflection. Due to adhesive interactions between the particles, the cantilever continues moving downward with the plate beyond its equilibrium position ($\Delta z = 0$). When the cantilever reaches a critical negative displacement (red marker in Fig.1d), the restoring elastic force exceeds the interparticle adhesive force F_c, leading to particle detachment. After detachment, the cantilever oscillates before returning to its equilibrium position. To determine the average adhesive force for a given contact, this procedure is repeated four times for each particle pair, corresponding to four successive times the cycle described in Fig.1d. Measurements are performed for 50 different particle pairs, resulting in a total of 200 measurements of F_c for each cohesive material.

3.4. Sensitivity analysis

In the protocol described above for measuring adhesive force, several experimental parameters may influence the measured force. We therefore first verified that the measured adhesive force is insensitive to the number of previous contacts between particles, the maximum normal load applied prior to detachment, the detachment velocity, and the contact time before detachment. Figure 2 summarizes four tests performed on CCGM particles with a diameter $d = 199\,\mu$m and a coating thickness $b = 65$ nm. The insets show the time evolution of the force corresponding to the different experimental protocols.

The first test, shown in Fig.2a, indicates that the measured adhesive force remains unchanged after repeated loading cycles (30 detachments under identical loading conditions on the same contact). This suggests that repeated contacts do not significantly alter the coating properties. Figure 2b further demonstrates that the adhesive force is independent of the maximum normal load applied before detachment. Similarly, by varying the pulling velocity from 0.01 to 5 mm/s (Fig.2c) and the contact time from 0.1 to 500 s (Fig.2d), we observe that the adhesive force remains constant. These results indicate that over the investigated parameter ranges, the adhesive force is primarily determined by the particle and coating properties.

Unless otherwise specified, all subsequent experiments were performed with a normal load of 40μN and a detachment velocity of 20 μm/s.

3.5. Results for the adhesion force

Figure 3 presents adhesion force measurements performed on CCGM particles with coating thicknesses $b = 15, 34, 65, 100$ and 200 nm and particle diameters $d = 199$ and 350 μm. For each particle batch, a total of 200 measurements was

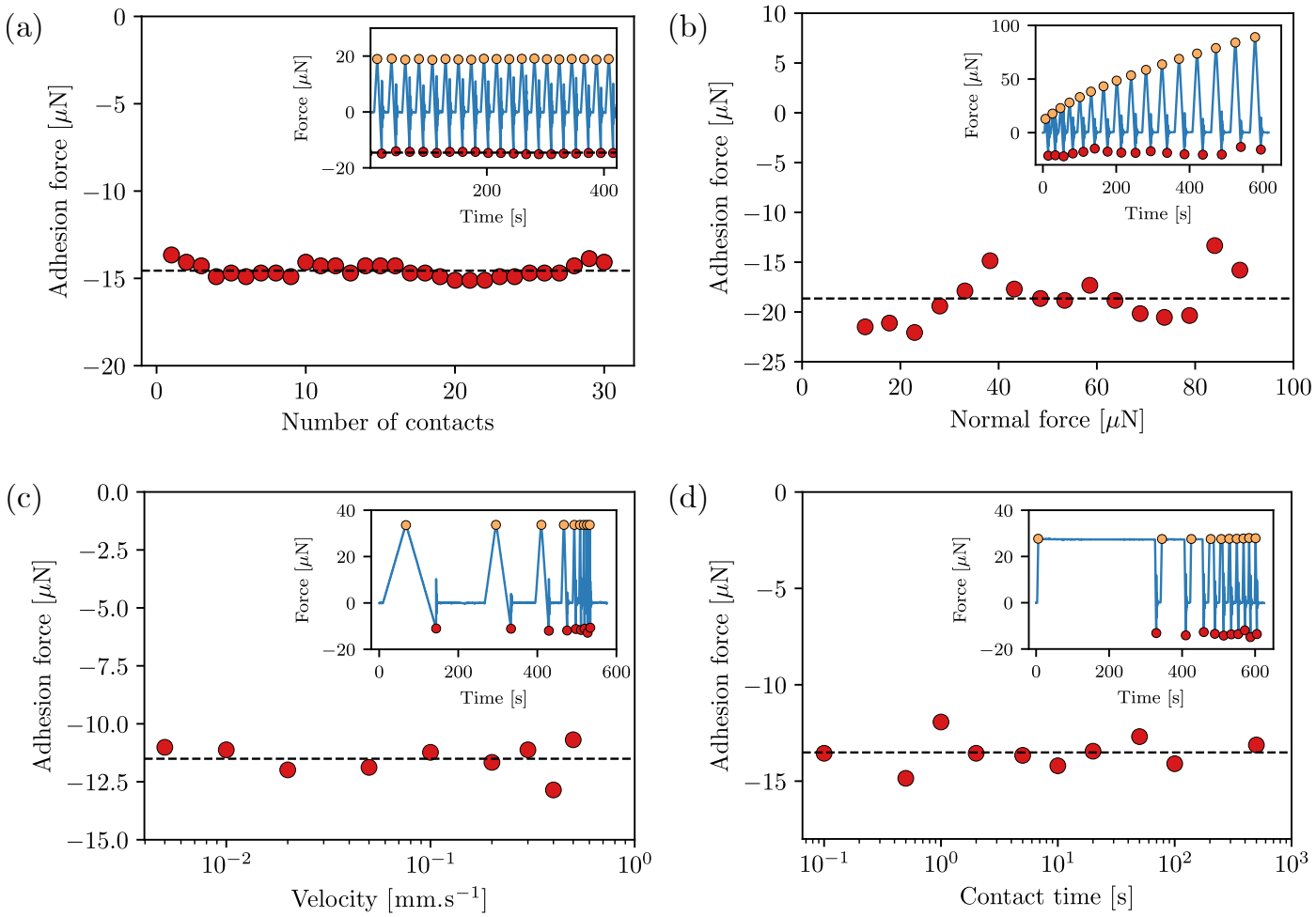

Figure 2: Adhesive force as a function of (a) the number of repeated contacts, (b) the normal loading force prior to detachment, (c) the pulling velocity, and (d) the contact time before detachment. All measurements were performed for coated particles with $d = 199\,\mu$m and $b = 65$ nm. Insets show the time evolution of the force, measured by the beam deflection, during the tests..

performed on different particle pairs. Figure 3a shows the resulting force distributions.

Except for the thinnest coating ($b = 15$ nm), for which a significant fraction of particle pairs exhibited no measurable adhesion, resulting in a peak at zero force, the measurements display approximately Gaussian force distributions. For each coating thickness, we fitted the distributions using a Gaussian function to extract the mean adhesion force $\langle F_c(b)\rangle$ and the distribution width $\delta F_c(b)$, which reflects heterogeneity in the coating thickness.

As shown in Fig.3b, increasing b both narrows the distributions and shifts them toward larger adhesion forces. Figure 3c shows the average adhesive force $\langle F_c(b)\rangle$ as a function of coating thickness b. The force increases with increasing b before reaching a plateau at large coating thickness. To compare the two particle sizes, we non-dimensionalize the data using the capillary force scale $3\pi\gamma d/2$, where the surface tension γ is chosen such that the normalized force approaches unity at large b. The results for the two particle sizes collapse onto a single curve, indicating that this capillary scaling captures the relevant physics. The data are well described by:

$$\langle F_c\rangle = \frac{3}{2}\pi\gamma d\left(1 - e^{-b/B}\right), \qquad (2)$$

where B is a characteristic length scale.

This behavior is similar to observations reported in [29] for larger particles ($d > 800\,\mu$m). The best fit yields $\gamma = 16$ mN/m and $B \approx 80$ nm.

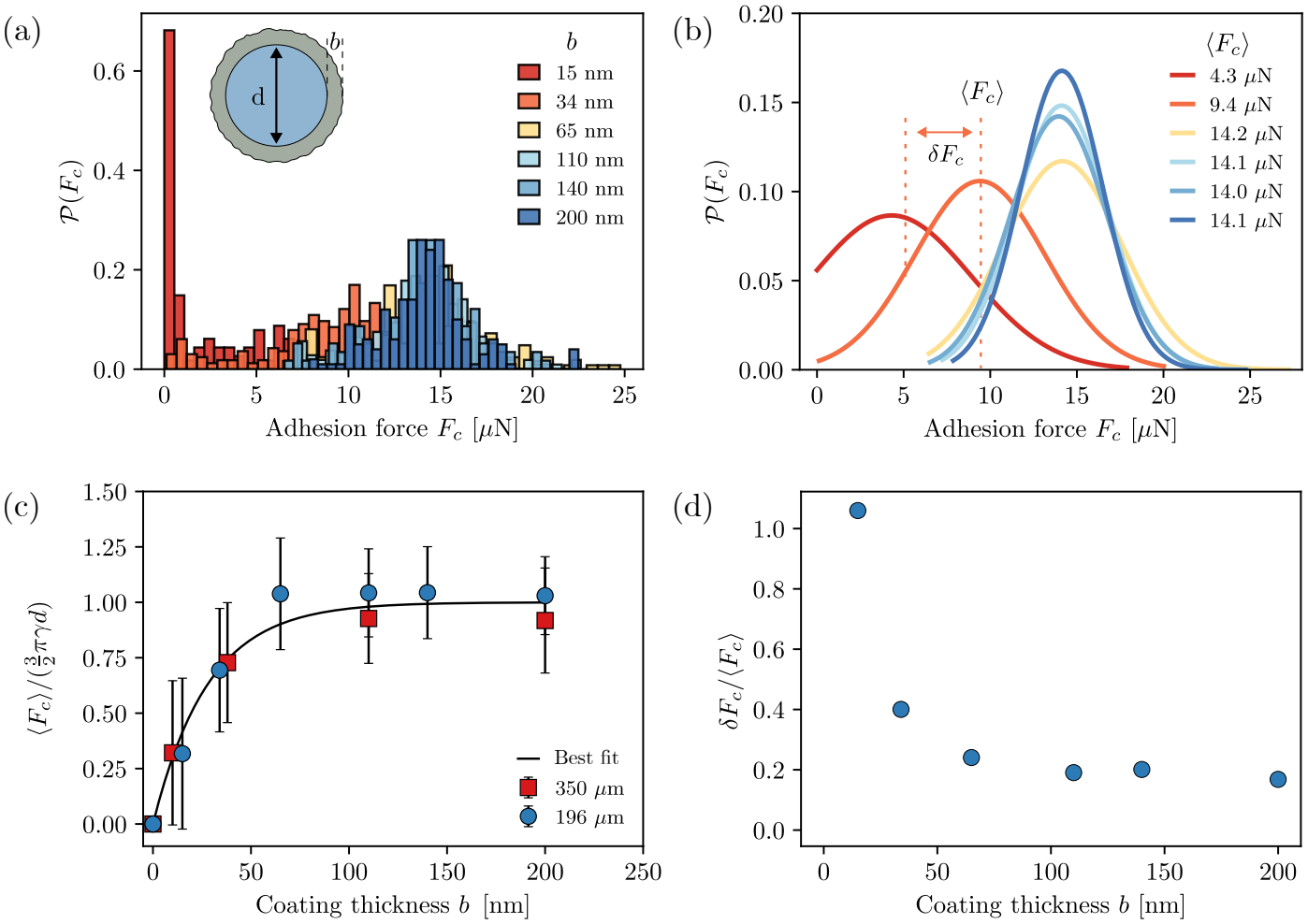

Figure 3: (a) Distribution of adhesive force $\mathcal{P}(F_c)$ for $d = 199\,\mu$m and different coating thicknesses b. (b) Corresponding Gaussian fits for each b. (c) Dimensionless average adhesive force as a function of b for $d = 199\,\mu$m (blue circles) and $350\,\mu$m (red squares); the solid line correspond to the fit given by Eq. (2) with $\gamma = 16$ mN/m and $B = 80$ nm. (d) Relative width of the distribution, $\delta F_c/\langle F_c \rangle$, as a function of b.

The value of γ is close to both the surface tension of PDMS and the value reported in [29]. However, B was previously found to be approximately 230 nm for larger particles. We attribute this difference to particle roughness: for our particles, we obtain an RMS roughness of approximately 25 nm (measured with AFM), which is smaller than that reported in [29].

Figure 3d shows the relative width of the force distribution $\delta F_c/\langle F_c \rangle$ as a function of b. It decreases from approximately 100% at low coating thickness to about 15% at large coating thicknesses. These results support the interpretation that increasing the coating thickness progressively fills surface asperities, thereby increasing the average adhesion force. Once the asperities are fully covered, particle contacts occur predominantly between polymer-coated surfaces, and further increases in coating thickness no longer increase the adhesion force.

4. Measuring Detachment Energy

Several numerical studies of the rheology of cohesive granular materials [24–27] or of the dynamics of fluidized beds [28] suggest that understanding their flow properties requires more than just knowledge of the interparticle adhesive force. The energy required to detach particles, which accounts for both the range of adhesive interaction and dissipative processes during detachment, may also be a crucial

microscopic quantity to consider. In this section, we demonstrate how our cantilever setup can be adapted to operate in a "catapult" mode, providing access to the detachment energy. The principle involves launching a particle attached to another at a given velocity and determining whether the initial kinetic energy is sufficient to break the adhesive bond.

4.1. From a cantilever to a controlled catapult

The measurement principle and protocol used to determine the detachment energy are illustrated in Fig.4. First, one particle is attached to the cantilever tip, while a second free particle is brought into contact with it and held in place solely by adhesive forces (Step 1). The cantilever is then bent upward to an initial displacement Δz_i using a horizontal razor blade mounted on a piezo actuator (Step 2). The blade is subsequently retracted, allowing the cantilever to accelerate downward until it impacts a vertical razor blade, which abruptly stops its motion (Step 3). If the initial deflection Δz_i is sufficiently large, the kinetic energy of the particle immediately before impact exceeds the adhesive energy binding the particles together, causing the lower particle to detach. The detachment energy E_{detach} is defined as the minimum kinetic energy required for particle detachment. To achieve sufficiently high velocities capable of overcoming the adhesive interactions investigated here, a cantilever stiffer than the one used for force measurements was used: a glass beam with a thickness of 550 μm and a length of approximately 6 cm.

To accurately characterize the particle dynamics, the side camera was replaced with a high-speed camera (Phantom v7) equipped with a Z16 LEICA lens, recording the detachment process at 24,000 frames per second. The positions of both particles were tracked using a Hough-transform-based algorithm [36], with sub-pixel accuracy achieved through a Gaussian fit to detect the peak intensity at the center of the grains (Fig.4c).

Typical tracked trajectories are shown in Fig.4d. The red curve represents the position of the particle attached to the cantilever, which accelerates and then rebounds after impact at $t = 0$. The second blue curve corresponds to the free particle launched after the impact. The first phase ($t < 0$, pink zone) corresponds to the acceleration phase prior to impact, during which the particles remain attached. The second phase (blue region) corresponds to the post-detachment trajectory, where the launched particle follows free-fall motion. The launch velocity v_i is controlled by the initial cantilever deflection Δz_i, as shown in the inset of Fig.4d.

The detachment process is associated with an abrupt change in velocity, as shown in Fig.4e, where the particle velocity (obtained by differentiating its position) is plotted as a function of time. The velocity of the particle, initially attached to the cantilever, first increases linearly during the beam acceleration, then undergoes a sudden drop during impact, and subsequently evolves under gravity.

The detachment process itself is very rapid and occurs on length and time scales not captured by our measurements. However, from the data, we can determine the velocity just before impact, v_i, and the final velocity just after detachment, v_f, by fitting the trajectories with a uniformly accelerated equation of motion, as depicted by the dashed lines in Fig.4d and e.

4.2. Results for the detachment energy

Here, we present energy measurements for CCGM particles with a diameter $d = 199$ μm and coating thicknesses $b = 34$, 65, 110, and 140 nm. For each value of b, more than 50 catapult experiments were conducted, varying the impact velocity v_i by adjusting the initial deflection of the cantilever. Figure 5a displays the trajectories of the launched particle for varying initial cantilever bending. Both the pre-impact velocity v_i and post-impact velocity v_f increase with greater initial bending.

Figure 5b shows how the post-impact velocity v_f varies with the impact velocity v_i. The different symbols correspond to different coating thicknesses. The filled symbols represent experiments where the grains detached, while the empty symbols represent experiments where

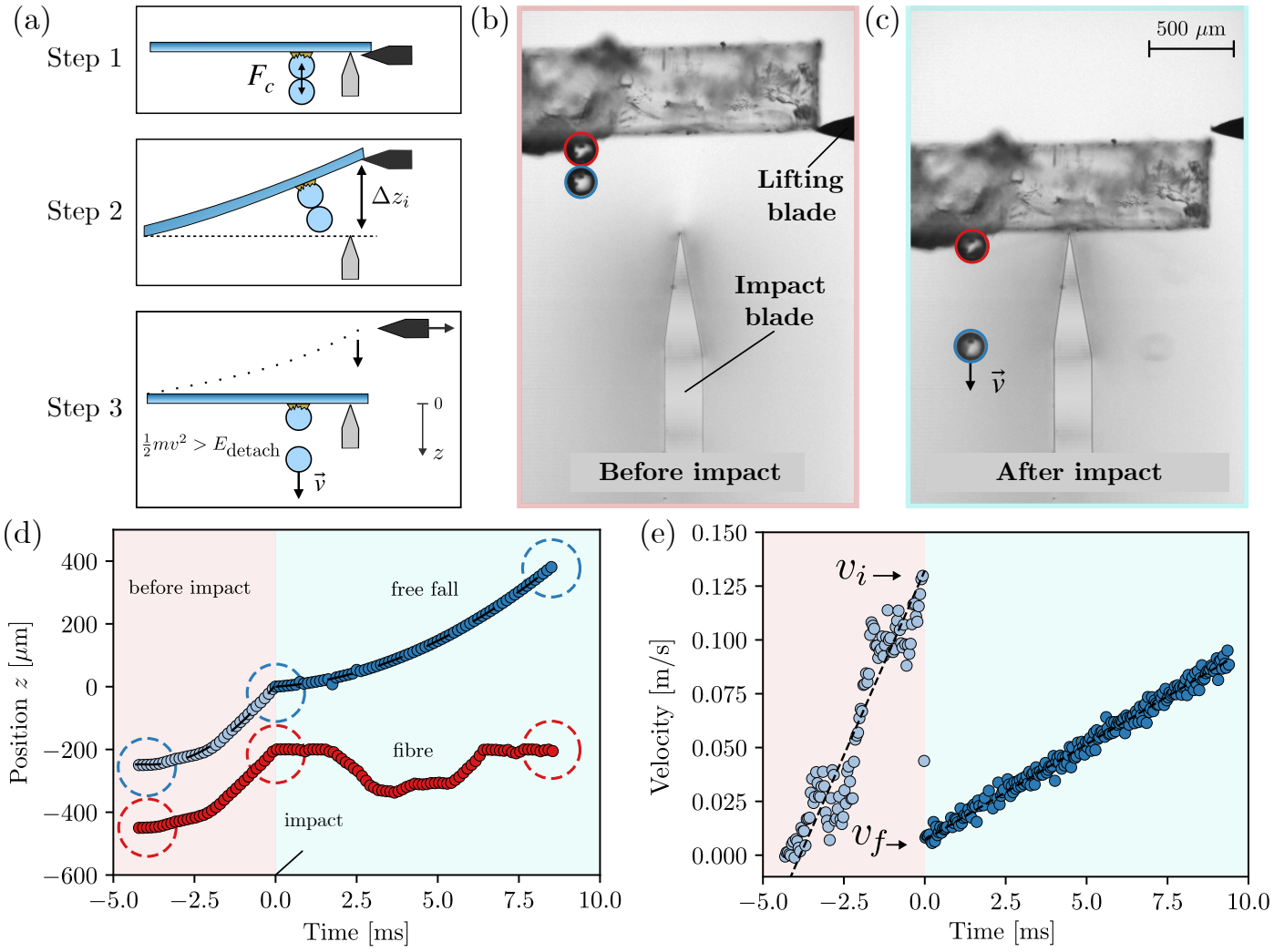

Figure 4: (a) Sketch of the catapult experiment; Step 1: a pair of particles is attached to the cantilever; Step 2: the beam is bent to an initial vertical deflection Δz_i; Step 3: the beam is suddenly released and impacts a fixed blade. (b, c) Images of the setup corresponding to Step 2 (prior to impact) and Step 3 (after impact). (d) Positions of the launched particle (blue) and the fixed particle (red) as a function of time; $t = 0$ corresponds to the time of impact. (e) Velocity of the launched particle as a function of time (derivative of data from (d)).

the initial kinetic energy was insufficient and the grains remained attached. Although there is relatively wide dispersion in the data, likely due to the heterogeneity of the coating, we systematically observe that the post-impact velocity becomes non-zero at a finite impact velocity and, on average, increases above this critical value.

Close to the detachment threshold, when v_f is small, the energy dissipated during detachment may be considered constant. Hence, to determine the minimal impact velocity v_0 required for detachment, we fit the data with a square root function $v_f = \sqrt{v_i^2 - v_0^2}$ (doted line in Fig. 5b), and the detachment energy is then estimated as $E_{\text{detach}} = \frac{1}{2}mv_0^2$.

Figure 5c shows how the detachment energy varies with the coating thickness b. In contrast to the adhesive force, which saturates for $b \gtrsim 60$ nm (inset of Fig.5c), the detachment energy continuously increases with b for all values investigated here. These results demonstrate that force and energy are distinct quantities, as energy is highly sensitive to dissipation mechanisms. Characterizing both is essential for a comprehensive understanding of the adhesion

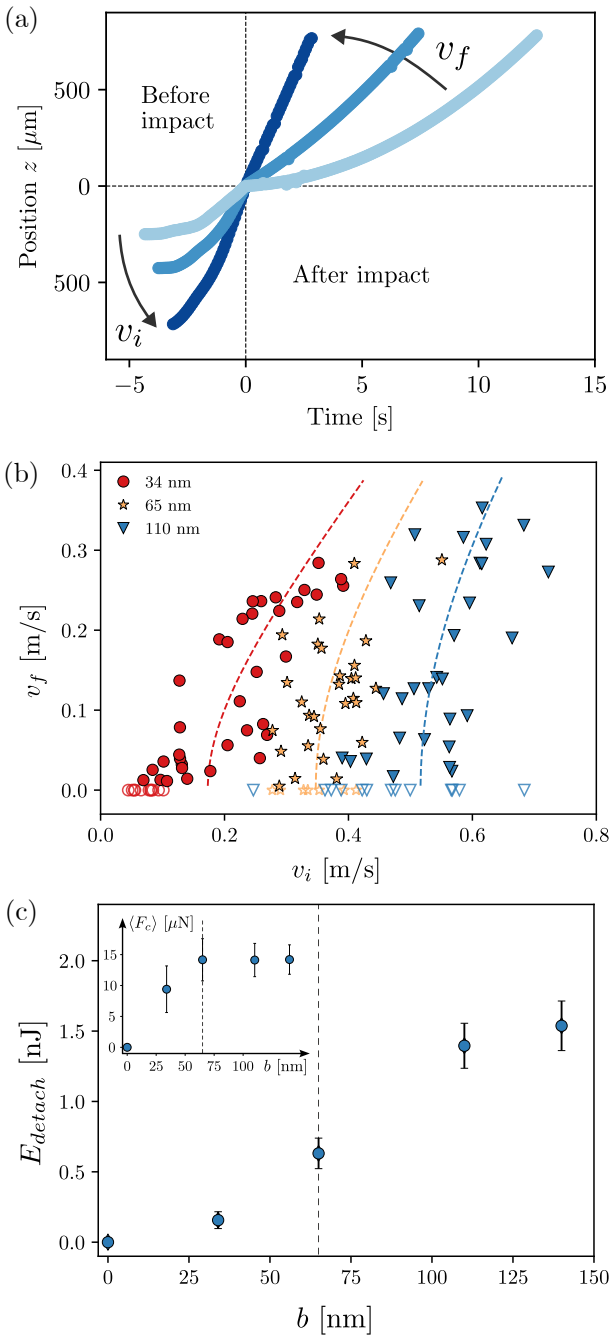

Figure 5: (a) Position of the launched particle vs time for an increasing initial bending of the cantilever from light to dark blue. (b) Velocity just after impact, v_f, as a function of the pre-impact velocity v_i. Dashed lines represent fits using the square root function $v_f = \sqrt{v_i^2 - v_0^2}$. c) Detachment energy $E_{detach} = \frac{1}{2}mv_0^2$ as a function of the coating thickness b for $d = 199$ μm; inset: average adhesive force $\langle F_c \rangle$ for comparaison.

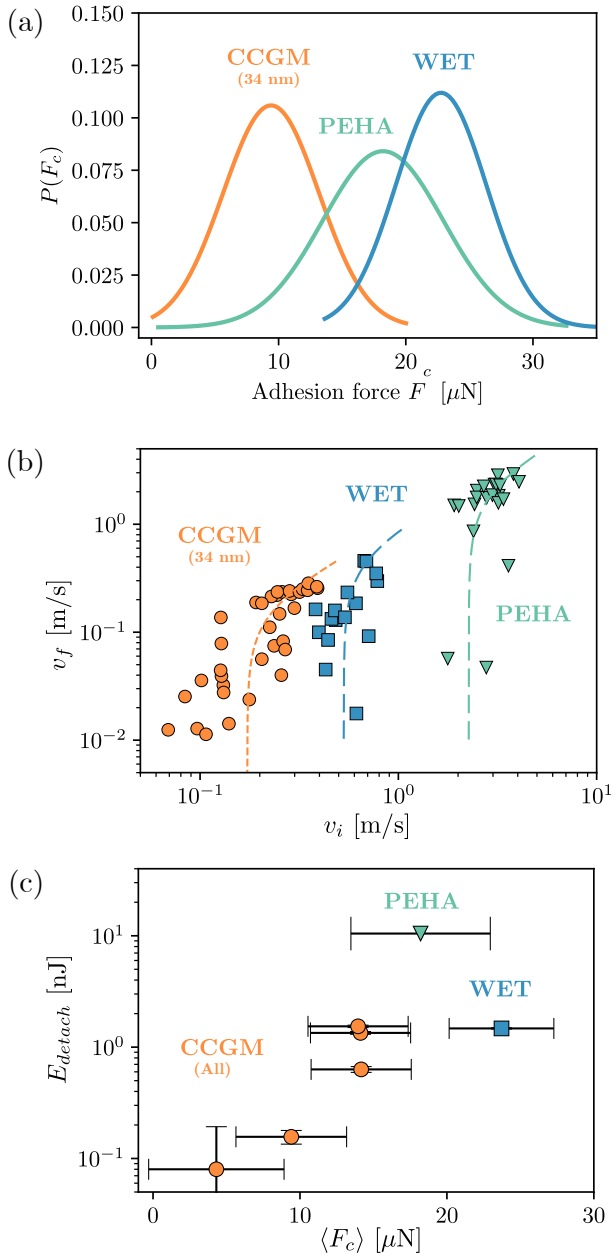

Figure 6: Comparison between the three types of particles: CCGM particles($b = 34$ nm), wet particles and PEHA particles. (a) Gaussian fits of the adhesive force distributions.(b) Final velocity after being catapulted as a function of the impact velocity. c) Detachment energy as a function of the adhesive force for all the particles tested in this study. The orange dots correspond to different CCGM (15, 34, 65, 110 and 140 nm, from bottom to top).

properties of cohesive powders.

4.3. Origin of the detachment energy

We define the detachment energy as the minimum kinetic energy required to separate the particles. While this quantity is experimentally well-defined, its interpretation is more complex. We anticipate that this energy has two main

contributions: first, the work done by the adhesive force over the typical detachment distance, which, in the case of our coated particles, corresponds to the average coating thickness b; and second, the energy dissipated during detachment, which arises from the stretching and breaking of the polymer film at the interface between the two particles. Hence, the detachment energy measures the coupled effect of both conservative (adhesion) and non-conservative forces (viscoelastic dissipation and plastic deformation).

Using the values obtained experimentally in Section 3, the order of magnitude for the typical work of adhesion, $F_c \times b$, is approximately 10^{-12} J, which is about 1000 times smaller than the typical detachment energy we measured. This suggests that the detachment process in the CCGM particles is primarily controlled by dissipation rather than the work of adhesion.

To better understand the dynamics of detachment, we present in Appendix C a theoretical model for the separation of two particles connected by a thin viscoelastic bridge. In this model, the fluid is treated as a Maxwell liquid, and the geometry of the bridge is simplified to a cylinder connecting the two particles. An empirical model is introduced to describe the transition of the liquid elongation from a thin layer (governed by lubrication equations) to an elongated filament before rupture.

Under these assumptions, the model captures the existence of two regimes, depending on the initial relative velocity of the particles. At low velocities, the launched particle initially moves away but is pulled back and remains attached to the other grain. At high velocities, the particle detaches and moves indefinitely away from the other grain. Using rheological properties from the literature for the PBS coating and assuming that the initial volume of the capillary bridge is equal to the total volume of coating around the particles, the model reproduces the order of magnitude of the critical detachment velocity measured in the experiments. However, it remains unclear whether, in our experiments, detachment occurs through the elongation of a viscoelastic bridge or by fracture, which would require a different modeling approach beyond the scope of this paper.

5. Comparison Between Different Cohesive Materials

In this final section, we apply the cantilever and catapult methods to measure the adhesive force distribution as well as the detachment energy for two other cohesive materials introduced in Section 2: wet granular materials and cross-linked PEHA polymer particles.

Figure 6a compares the force distributions for wet grains and PEHA particles with CCGM particles ($b = 34$ nm). For all three materials, the adhesive force is of the same order of magnitude, with the wet particles being the most adhesive, followed by the PEHA particles, which are slightly more adhesive than the CCGM coated particles. The shift between CCGM and wet particles could come from difference in surface tension, which is higher for the glycerol mixture (60 mN.m^{-1}) than for PDMS (20 mN.m^{-1}). The origin of adhesion for the PEHA particles is more complex to interpret. It may result from the deformability of the rubbery microparticles and the intricate interactions between the dangling chains from the polymer network at the surface of the synthesized microparticles.

In Fig.6b, we present the results of the catapult experiments, comparing how the post-impact velocity varies with the initial velocity for the three materials. In contrast to the adhesive force, the detachment energies measured for the different materials differ by more than one order of magnitude. The PEHA particles require a significantly higher initial kinetic energy to detach compared to the wet grains, which in turn require more energy to detach than the 34 nm coated CCGM particles. Figure 6c summarizes these findings in a force-energy diagram for the materials tested in this study, demonstrating that these materials cover a relatively wide range of parameters.

6. Conclusion

This study presents an innovative and versatile cantilever-based method to characterize interparticle adhesion in cohesive granular materials. Importantly, the method bridges a critical gap by enabling adhesion measurements for particle sizes in the range of 100 μm to 1 mm, where standard AFM-based methods are hardly applicable. Additionally, it allows for measurements across a large number of particle pairs, which is crucial for obtaining statistically relevant data. By combining a glass-beam cantilever for force measurements with a novel catapult mode for energy measurements, the method provides access to two complementary adhesive properties: the detachment force and the detachment energy.

To demonstrate the versatility and range of applicability of the method, we applied it to three distinct cohesive materials: polymer-coated particles (CCGM), wet granular media, and low-T_g cross-linked polymer microparticles. For CCGM particles, the adhesive force follows a capillary scaling with coating thickness and saturates beyond a characteristic coating thickness, consistently across two particle sizes. By contrast, the detachment energy continues to grow with coating thickness well beyond this saturation point, highlighting the fundamental decoupling between force and energy as complementary adhesive properties. Across the three materials tested, the adhesive force is multiplied by a factor 5, whereas the detachment energy span nearly over two orders of magnitude, demonstrating that these model materials cover a wide range of adhesive parameters, which could be of interest for future studies investigating their bulk properties.

Importantly, this method opens new avenues for connecting microscopic adhesive properties to macroscopic flow behavior in cohesive granular media. The ability to independently measure the detachment force and detachment energy will be crucial for identifying the role of each interparticle adhesive property in the different regimes of cohesive rheology. This may be the key to shedding light on the physical origin of powder flowability, ultimately advancing both fundamental understanding and practical applications in industries where cohesive powders play a central role.

CRediT Author Statement

- M. Lajeunesse: Methodology, Investigation, Data Curation, Formal Analysis, Writing-Original Draft.
- F. M. Rocha: Conceptualization, Supervision, Writing-Review & Editing.
- D. Dumont: Methodology, Formal Analysis, Writing-Review & Editing.
- V. Bertin: Methodology, Formal Analysis, Writing-Review & Editing.
- Y. Moratille: Resources.
- N. Sintès-Zydowicz: Resources, Writing-Review & Editing.
- E. Drockenmuller: Resources, Writing-Review & Editing.
- O. Pouliquen: Conceptualization, Funding Acquisition, Supervision, Writing-Review & Editing.

Acknowledgments

This work greatly benefited from discussions with A. Asnacios, who advised us on the cantilever setup, and with M. Nicolas. We also thank A. Fruh, B. Bresson, and J. Comtet for their help in performing a few AFM experiments. This project has received funding from the European Research Council (ERC) under the European Union's Horizon Europe programme (Grant No. 101097842). The authors also acknowledge financial support from the International Fine Particle Research Institute (IFPRI) and the Agence Nationale de la Recherche under the RheoCom project (Grant No. ANR-22-CE06-0020). Views and opinions

expressed are, however, those of the author(s) only and do not necessarily reflect those of the European Union or the European Research Council. Neither the European Union nor the granting authority can be held responsible for them.

References

[1] K. Kamrin, K. Hill, D. Goldman, J. Andrade, Advances in modeling dense granular media, Annu. Rev. Fluid Mech. 56 (2024) 215–240.

[2] P. Rognon, J. Roux, D. Wolf, M. Naaïm, F. Chevoir, Rheophysics of cohesive granular materials, Europhys. Lett. 74 (2006) 644.

[3] M. Badetti, A. Fall, D. H. F., Chevoir, P. Aimedieu, S. Rodts, J. Roux, Rheology and microstructure of unsaturated wet granular materials: Experiments and simulations, J. Rheol. 62 (2018) 1175–1186.

[4] T. Vo, S. Nezamabadi, P. Mutabaruka, J. Delenne, F. Radjai, Additive rheology of complex granular flows, Nat. Commun. 11 (2020) 1476.

[5] O. Pouliquen, Powders and cohesive granular media: a rheological perspective, Rheol. Acta 64 (2025) 195–207.

[6] Q. Li, V. Rudolph, B. Weigl, A. Earl, Interparticle van der waals force in powder flowability and compactibility, Int. J. Pharm. 280 (2004) 77–93.

[7] A. Castellanos, The relationship between attractive interparticle forces and bulk behaviour in dry and uncharged fine powders, Adv. Phys. 54 (2005) 263–376. doi:10.1080/17461390500402657.

[8] G. Lumay, F. Boschini, K. Traina, S. Bontempi, J. Remy, R. Cloots, N. Vandewalle, Measuring the flowing properties of powders and grains, Powder technol. 224 (2012) 19–27.

[9] R. Sharma, A. Sauret, Experimental models for cohesive granular materials: a review, Soft Matter 21 (2025) 2193–2208.

[10] O. Pitois, P. Moucheront, X. Chateau, Liquid bridge between two moving spheres: an experimental study of viscosity effects, J. Colloid Interface Sci. 231 (2000) 26–31.

[11] W. Ducker, T. Senden, R. Pashley, Direct measurement of colloidal forces using an atomic force microscope, Nature 353 (1991) 239–241.

[12] M. Kappl, H. Butt, The colloidal probe technique and its application to adhesion force measurements, Part. Part. Syst. Charact. 19 (2002) 129–143.

[13] S. Scherrer, S. Ramakrishna, V. Niggel, N. Spencer, L. Isa, Measuring rolling friction at the nanoscale, Langmuir 40 (2024) 6750–6760.

[14] R. Jones, H. Pollock, D. Geldart, A. Verlinden, Interparticle forces in cohesive powders studied by afm: effects of relative humidity, particle size and wall adhesion, Powder Technol. 132 (2003) 196–210.

[15] R. Fuchs, T. Weinhart, J. Meyer, H. Zhuang, T. Staedler, X. Jiang, S. Luding, Rolling, sliding and torsion of micron-sized silica particles: experimental, numerical and theoretical analysis, Granul. matter 16 (2014) 281–297.

[16] M.-J. Colbert, M. Grandbois, N. Abatzoglou, Identification of inter-particular forces by atomic force microscopy and how they relate to powder rheological properties measured in shearing tests, Powder Techno. 284 (2015) 396–402.

[17] S. Booth, J. Newton, Experimental investigation of adhesion between powders and surfaces, J. Pharm. Pharmacol. 39 (1987) 679–684.

[18] F. Podczeck, J. Newton, Development of an ultracentrifuge technique to determine the adhesion and friction properties between particles and surfaces, J. Pharm. Sci. 84 (1995) 1067–1071.

[19] S. Wanka, M. Kappl, M. Wolkenhauer, H. Butt, Measuring adhesion forces in powder collectives by inertial detachment, Langmuir 29 (2013) 16075–16083.

[20] T. Deng, V. Garg, M. Bradley, A study of particle adhesion for cohesive powders using a novel mechanical surface energy tester, Powder Technol. 391 (2021) 46–56.

[21] L. Pedrolli, S. Nadimi, S. Maramizonouz, B. Menor, A. López, Kinetic adhesion test to determine particle surface energy, HardwareX 14 (2023) e00437.

[22] J. Israelachvili, Intermolecular and surface forces, Academic press, 2011.

[23] N. Desprat, A. Guiroy, A. Asnacios, Microplates-based rheometer for a single living cell, Rev. Sci. Instrum. 77 (2006).

[24] S. Roy, A. Singh, S. Luding, T. Weinhart, Micro–macro transition and simplified contact models for wet granular materials, Comput. Part. Mech. 3 (2016) 449–462.

[25] S. Mandal, M. Nicolas, O. Pouliquen, Insights into the rheology of cohesive granular media, Proceedings of the National Academy of Sciences 117 (2020) 8366–8373.

[26] S. Mandal, M. Nicolas, O. Pouliquen, Rheology of cohesive granular media: Shear banding, hysteresis, and nonlocal effects, Phys. Rev. X 11 (2021) 021017.

[27] M. Macaulay, P. Rognon, Viscosity of cohesive granular flows, Soft matter 17 (2021) 165–173.

[28] W. LaMarche, P. Liu, K. Kellogg, A. Lattanzi, C. Hrenya, Toward general regime maps for cohesive-particle flows: Force versus energy-based descriptions and relevant dimensionless groups, AIChE Journal 67 (2021) e17337.

[29] A.Gans, O. Pouliquen, M. Nicolas, Cohesion-controlled granular material, Phys. Rev. E 101 (2020) 032904.

[30] S. Herminghaus, Dynamics of wet granular matter, Adv. Phys. 54 (2005) 221–261.
[31] N. Mitarai, F. Nori, Wet granular materials, Adv. Phys. 55 (2006) 1–45.
[32] M. Scheel, R. Seemann, M. Brinkmann, M. D. Michiel, A. Sheppard, S. Herminghaus, Liquid distribution and cohesion in wet granular assemblies beyond the capillary bridge regime, J. Phys.: Condens. Matter 20 (2008) 494236.
[33] Y. Moratille, M. Arshad, C. Cohen, A. Maali, E. Lemaire, N. Sintes-Zydowicz, E. Drockenmuller, Cross-linked polymer microparticles with tunable surface properties by the combination of suspension free radical copolymerization and click chemistry, J. Colloid Interface Sci. 607 (2022) 1687–1698.
[34] P. Wu, D. Aroush, A. Asnacios, W. Chen, M. Dokukin, B. Doss, P. Durand-Smet, A. Ekpenyong, J. Guck, N. Guz, A comparison of methods to assess cell mechanical properties, Nat. Methods 15 (2018) 491–498.
[35] C. Truesdell, The rational mechanics of flexible or elastic bodies 1638–1788, Springer, 1960.
[36] W. Yang, Z. Huang, Fast circular object detection using multiscale grayscale hough transform, Appl. Mech. Mater. 490 (2014) 1542–1547.

Appendix A. Coating of CCGM particles

We summarize here the protocol [29], to prepare the coated silica particles (CCGM) characterised in the adhesion experiments.

In this process, we used silica particles with a mean diameter of $d = 199 \pm 16$ μm as shown by the distribution from Fig.A.7(b). First, 1 kg of dry silica particles is weighed in a large metal bowl. A sample of 50–100 g of particles is then transferred to a small glass container. Using a precision balance, a predetermined mass m_{pdms} of hydroxy-terminated PDMS (with viscosity 750 cSt, Fig.A.7(a)) is introduced into the glass container using a syringe pump. The PDMS is poured at the center of the container to prevent contact between the liquid and the container walls, thereby minimizing material loss. The mass of PDMS is calculated to produce a target coating thickness b over the entire 1 kg batch of silica particles, assuming a homogeneous coating layer.

The particles containing the PDMS are then transferred back into the large metal bowl and mixed with the remaining silica particles. To cross-link the PDMS, a boric acid solution is prepared by dissolving a mass of boric acid powder corresponding to $m_{bore} = 0.14 \times m_{pdms}$ in 100 mL of purified water at 60°C [29]. The solution is stirred for 5 min until homogeneous and is subsequently added to the metal bowl containing the silica particles and PDMS.

The mixture is then stirred for 90 mintues in a mixer maintained at 110°C to promote cross-linking of the polymer while simultaneously evaporating the water. At the end of the process, the PDMS is covalently cross-linked into polyborosiloxane (PBS) depicted in Fig.A.7(b), hence forming a quasi-homogeneous coating around the silica particles.

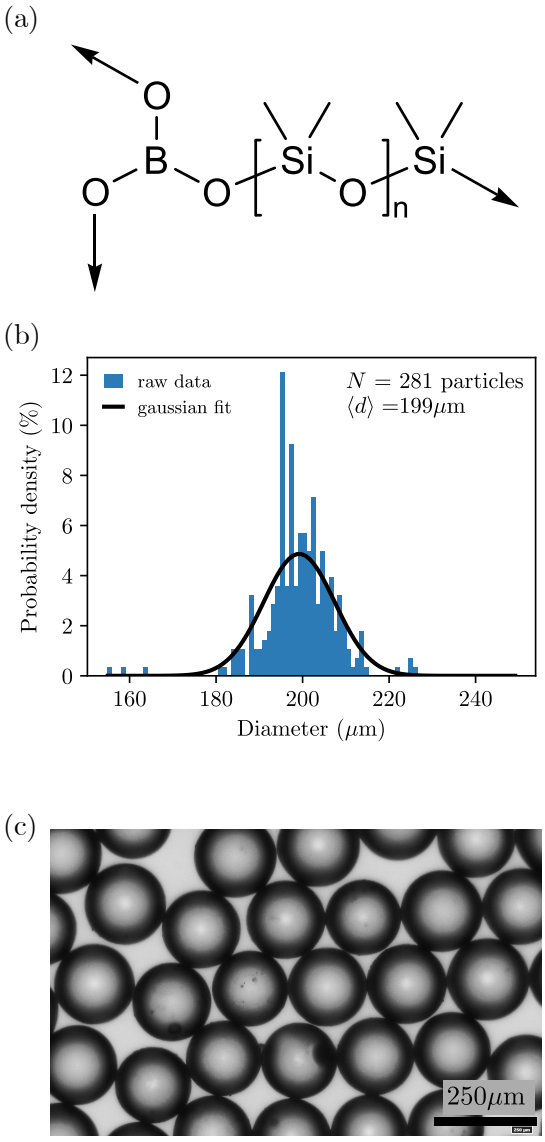

Figure A.7: (a) Chemical structure of cross-linked polyborosiloxane (PBS), (b) Size distribution of our particles (c) Image of CCGM particles (110 nm).

Appendix B. Synthesis of PEHA microparticles

We present here an extension of the protocol developed in [33] using membrane emulsification-assisted suspension radical copolymerization, to prepare the soft polymer particles characterised in the adhesion experiments.

The cross-linked PEHA (Fig.B.8(a)) microparticles were prepared by radical copolymerization in suspension in a double-walled glass reactor equipped with a 6-blade stirrer, a condenser and a thermometer (Fig. B.8(a)). The emulsion was formed by membrane emulsification (Dispersion Cell, Micropore Technology Ltd) using a hydrophilic metal membrane with pores 100 μm in diameter, an injection base, an emulsification cell, and a two-blade stirring module equipped with a PTFE vortex breaker and powered by a 24 V motor (DC INSTEK Model PR 3060). The injection of the monomer phase through the membrane was performed using a syringe pump (KDS100 Legacy, Fisher Scientific). The continuous aqueous phase containing poly(vinyl alcohol) (PVA, Mw = 70 kg.mol^{-1}, 88% hydrolyzed, 0.32 g, 4.0 g.L^{-1}) dissolved in distilled water (80 mL) and the dispersed monomer phase containing a mixture of 2-ethylhexyl acrylate (15.7 g, 85.3 mmol), 1,6-hexanediol dimethacrylate (1.14 g, 5.02 mmol), propargyl acrylate (1.11 g, 10.0 mmol), and lauroyl peroxide (0.40 g, 1.01 mmol) were degassed separately by argon bubbling during 15 min. The monomer phase was then injected into the aqueous phase through the metal membrane at a flow rate of 2 mL.min^{-1} and a constant stirring of 800 rpm. The emulsion was then transferred from the membrane emulsification device to the reactor, and the copolymerization was carried-out for 5 h at 60 °C under an argon flow and a stirring of 200 rpm. The reaction mixture was then cooled down, and the microparticles were isolated through several cycles of centrifugation (10 000 rpm) and dispersion in ethanol (3 × 100 mL) and distilled water (5 × 100 mL) to remove residual traces of comonomers and the PVA adsorbed onto the surface of the microparticles. Finally, PEHA microparticles were freeze-dried and recovered as a compact white powder (15.1 g, 82.2%) (see Fig. B.8(c)-(d)).

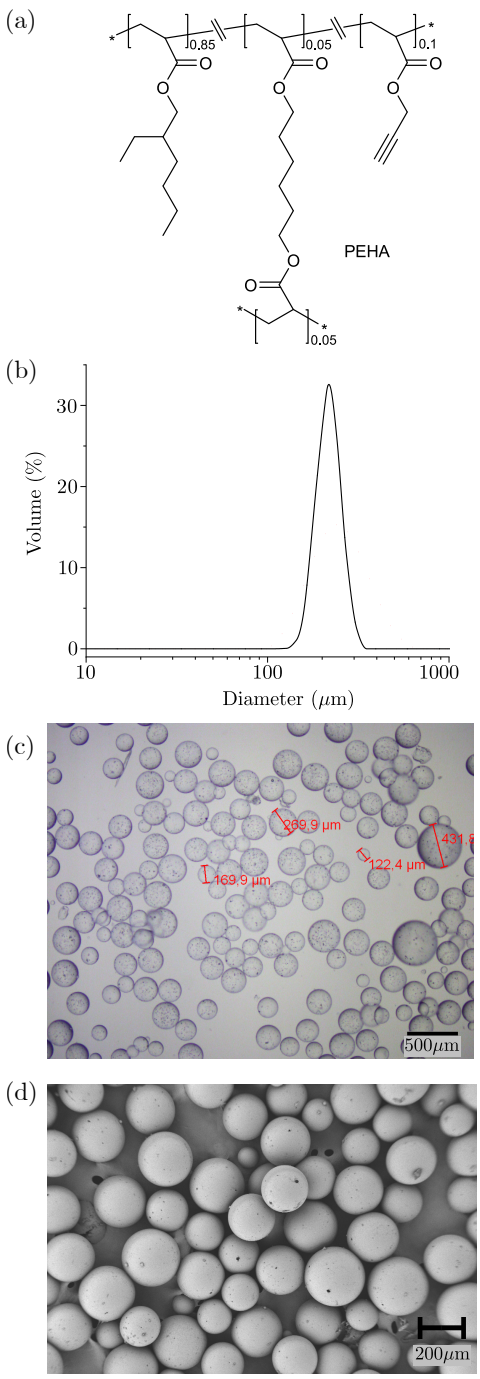

Figure B.8: (a) Chemical structure, (b) Light diffraction size distribution (Ø =232 µm, s = 0.63), (c) Optical microscopy, and (d) Scanning electron microscopy of PEHA microparticles.

Appendix C. Detachment of two particles linked by a viscoelastic bond

In this Appendix, we propose a model to estimate the detachment energy of two CCGM particles. In particular, we aim to rationalize the observed dependence of E_{detach} on the coating thickness (see Fig. 5(b-c)), whereas the quasi-static adhesion force becomes nearly independent of the coating thickness for sufficiently thick coatings (see Fig. 3(a-c)). To that end, we develop a minimal model accounting for viscoelastic dissipation during the detachment process.

Appendix C.1. Model geometry and momentum balance

We consider two spheres of radius R and mass m, linked by a capillary bridge of height $L(t)$ and wetting radius $a(t)$ (Fig. C.9(a)). The total volume of fluid in the bridge is denoted by V. When the two particles come into contact, the (negative) capillary pressure within the connecting liquid bridge draws polymer from the coating into the contact region. In what follows, we make the simplifying assumption that the volume of the capillary bridge corresponds to the total polymer coating volume of a single particle, with each particle contributing half of its coating to the bridge:

$$V = 4\pi R^2 b. \tag{C.1}$$

For the sake of simplicity, we further assume that the capillary bridge retains a cylindrical geometry throughout the separation process, such that volume conservation imposes

$$V = \pi a^2(t) L(t) \tag{C.2}$$

The liquid is assumed to behave as a viscoelastic fluid with density ρ, viscosity η, and relaxation time λ, while its surface tension and contact angle are denoted by γ and θ, respectively.

We consider the top particle to be fixed. The second particle is initially at a distance L_0 from the first and is launched with an initial velocity v_0. During its motion, the particle experiences two forces: a capillary force F_{cap} and a viscoelastic force F_{viscoel}. The momentum balance along the vertical axis therefore reads

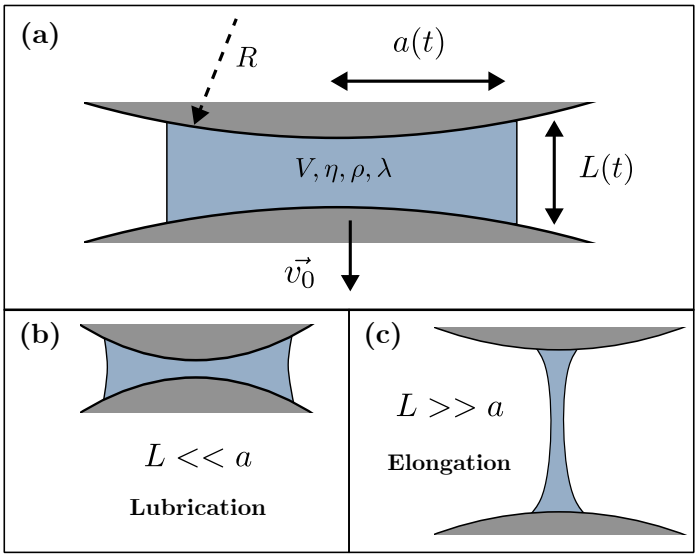

Figure C.9: Schematic of a simple capillary bridge between two rigid spheres.

$$m\frac{d^2L}{dt^2} = F_{cap} + F_{viscoel}. \tag{C.3}$$

The following two subsections provide models for these two forces.

Appendix C.2. Viscoelastic force

The viscoelastic force can be expressed as the average normal stress in the fluid, σ_{viscoel}, integrated over the wetted area:

$$F_{\text{viscoel}} = \pi a^2(t)\sigma_{\text{viscoel}} = \frac{V}{L(t)}\sigma_{\text{viscoel}}, \tag{C.4}$$

where volume conservation has been used.

During detachment, the bridge geometry evolves considerably, from a nearly flat thin film (Fig. C.9(b)), hereafter referred to as the *lubrication limit*, to a stretched slender ligament (Fig. C.9(c)), referred to as the *elongation limit*. The viscous resistance originates from different flow fields in these two limiting geometries.

In the lubrication limit, $L(t) \ll a(t)$, separation of the particles induces predominantly radial flow within the thin liquid layer. Lubrication theory gives the normal viscous force

$$F_{\text{lub}} = 6\pi\eta\left(\frac{R}{2}\right)^2 \frac{1}{L(t)}\frac{dL(t)}{dt}, \tag{C.5}$$

where $R/2$ is the reduced radius of two identical spheres. Dividing this force by the wetted area $\pi a^2(t) = V/L(t)$ gives the corresponding average stress,

$$\sigma_{\rm lub} = \frac{3}{2}\pi\eta R^2 \frac{1}{V}\frac{dL(t)}{dt}. \tag{C.6}$$

In the opposite elongation limit, $L(t) \gg a(t)$, the bridge behaves as a slender filament undergoing approximately uniaxial extension. For a Newtonian fluid, the corresponding extensional stress is

$$\sigma_{\rm elong} = 3\eta \frac{1}{L(t)}\frac{dL(t)}{dt}, \tag{C.7}$$

where the factor 3 is the Trouton ratio.

To describe the continuous transition between these two geometrical limits, we introduce the following interpolation for the instantaneous viscous stress:

$$\sigma_{\rm visc} = 3\eta \frac{1}{L(t)}\frac{dL(t)}{dt}\left[\frac{1}{1+\dfrac{2V}{\pi R^2 L(t)}}\right]. \tag{C.8}$$

This expression recovers the lubrication result for $L \ll a$ and the uniaxial elongation result for $L \gg a$. Investigating the denominator of (C.8), the typical length at which the transition from lubrication to elongation occurs is $2V/(\pi R^2)$.

Finally, to account for the viscoelasticity of the polymer coating, we assume a linear Maxwell rheology, such that the viscoelastic stress obeys

$$\lambda\frac{d\sigma_{\rm viscoel}}{dt} + \sigma_{\rm viscoel} = 3\eta \frac{1}{L(t)}\frac{dL(t)}{dt}\left[\frac{1}{1+\dfrac{2V}{\pi R^2 L(t)}}\right]. \tag{C.9}$$

Appendix C.3. Capillary force

The capillary force is maximal when the two particles are close. In the limit of vanishing separation, its characteristic magnitude is

$$F_{\rm cap}(L \to 0) = 2\pi\gamma R\cos\theta, \tag{C.10}$$

which corresponds to the classical capillary force between two identical spheres connected by a liquid bridge [10]. As the particles separate, the capillary force progressively decreases and eventually vanishes for a sufficiently elongated bridge. For the sake of simplicity, we use the same interpolation function as for the viscous stress to connect these two limits:

$$F_{\rm cap} = 2\pi\gamma R\cos\theta\left[1 - \frac{1}{1+\dfrac{2V}{\pi R^2 L(t)}}\right]. \tag{C.11}$$

This expression recovers the capillary force $2\pi\gamma R\cos\theta$ for $L \to 0$, and progressively vanishes as the bridge is elongated.

A similar approach was proposed by Pitois et al. [10] to describe the capillary and viscous forces between two spheres connected by a Newtonian liquid bridge. Their model is based on the lubrication limit, with finite-volume corrections accounting for the finite extent of the liquid bridge. Here, we use a slightly different interpolation, as our model also aims to recover the elongational-flow limit when the bridge becomes slender, $L \gg a$. In addition, the viscoelastic nature of the polymer coating is accounted for through the Maxwell constitutive equation introduced above.

Appendix C.4. Non-dimensionalization and numerical methods

Equations (C.3), (C.4), (C.9), and (C.11) form a closed set of equations. Together with the initial conditions $L(0) = L_0$ and $\dot{L}(0) = v_0$, they determine the dynamics of the launched particle.

To non-dimensionalize the equations, we define $X = L/L_c$, $t^* = t/\tau$, and $Y = \sigma/\sigma_0$, where the characteristic length L_c, inertio-capillary time scale τ, and stress σ_0 are given by

$$\begin{aligned} L_c &= \frac{V}{\pi R^2} \\ \tau &= \sqrt{\frac{mL_c}{2\pi\gamma\cos\theta R}} \\ \sigma_0 &= \frac{mL_c^2}{V\tau^2} \end{aligned} \tag{C.12}$$

In dimensionless form, the system of equations and initial conditions are

$$\begin{aligned}
&\ddot{X} + \left(1 - \frac{1}{1+2/X^2}\right) + \frac{Y}{X} = 0,\\
&\dot{Y} + \frac{\tau}{\lambda}\left[Y - \frac{3\eta}{\sigma_0\tau}\frac{\dot{X}}{X}\left(\frac{1}{1+2/X^2}\right)\right] = 0,\\
&\dot{X}(0) = V_0 = \frac{v_0\tau}{L_c},\\
&X(0) = \frac{L_0}{L_c}.
\end{aligned} \tag{C.13}$$

where dots now denote derivatives with respect to the dimensionless time t^*. The dynamics is therefore controlled by four dimensionless parameters: the Deborah number λ/τ, a dimensionless viscosity $3\eta/(\sigma_0\tau)$ comparing viscous and inertio-capillary effects, analogous to the Ohnesorge number in fluid dynamics, and lastly the dimensionless initial velocity $v_0\tau/L_c$ and initial distance L_0/L_c.

The system (C.13) is solved as an initial-value problem using a fourth-order Runge–Kutta scheme implemented in Python using scipy.integrate.

Appendix C.5. Prediction of the model

The parameters of the viscoelastic material are taken from the data provided in [29] and are fixed as $\rho_l = 970\,\mathrm{kg\,m^{-3}}$, $\gamma = 0.020\,\mathrm{N\,m^{-1}}$, and $\lambda = 3.8\,\mathrm{s}$. The choice is less obvious for the viscosity of the cross-linked PBS coating, which is usually very high, typically between $10^3 - 10^4$ Pa s, as it is strain-dependent. Here, we use $\eta = 4000$ Pa.s. The initial length of the liquid is taken to be equal to the coating thickness, typically $b = 110$ nm in the data presented here, which defines its dimensionless value as $X_0 = b/L_c$. The total volume of the bridge is then given by $V = 4\pi R^2 b$.

The results are shown in Fig. C.10(a)–(c), where each colour corresponds to a different initial velocity v_0. We identify two regimes: either the particle remains attached and returns to its initial position at $X = 0$, or it escapes. The transition appears clearly when plotting the velocity as a function of time, as shown in Fig.C.10(b), or in the phase space of the trajectory, plotting $\dot{X}$ as a function of X. A velocity that tends to a positive constant indicates that the particle detaches, while a negative value indicates that the particle remains attached. Note that we stop the simulation when the particle returns to $X = 0$, as we do not model the collision. As shown in Fig. C.10(d), the model reproduces the order of magnitude of the critical detachment velocity and qualitatively recovers its increase with coating thickness.

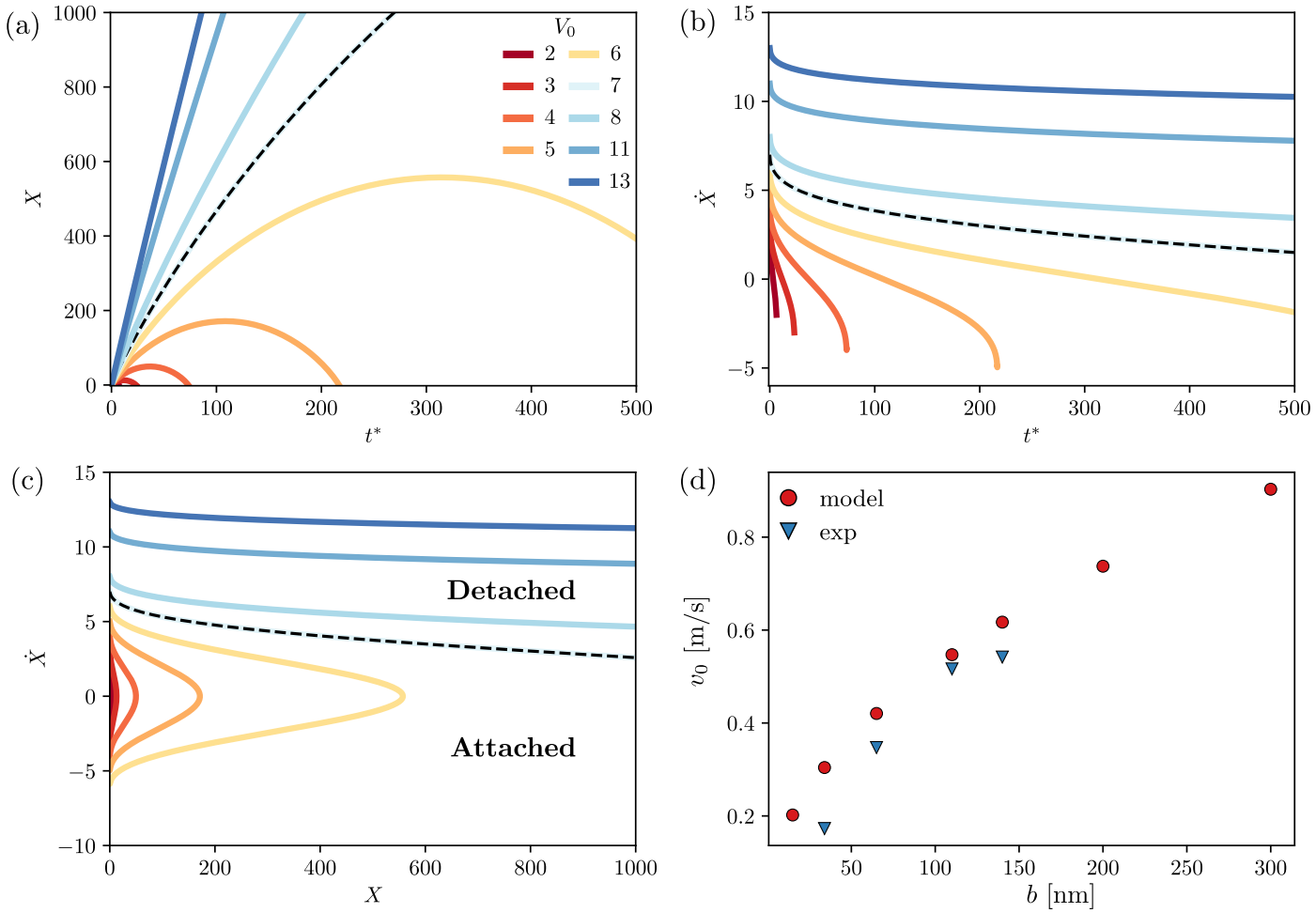

Figure C.10: (a) Dimensioness position as function of dimensionless time. The trajectories are parabolic if the grain remains attached. (b) Velocity as function of time. The dotted black line represent the seperatrix between the two regimes. (c) Phase diagram showing velocity as function of position. (d) Escape velocities versus coating thickness, comparing the theoretical predictions of the model to the real catapult experiments.